Clinical and Translational Radiation Oncology 52 (2025) 100940

Contents lists available at ScienceDirect

Clinical and Translational Radiation Oncology

journal homepage: www.sciencedirect.com/journal/clinical-and-translational-radiation-oncology

Magnetic resonance imaging to detect tumor hypoxia in brain malignant disease: A systematic review of validation studies

Y. Bai [a], E.C. Osmundson [b], M.J. Donahue [c,d,e], J.B. De Vis [f,*]

[a] Vanderbilt School of Medicine, Vanderbilt University, Nashville, TN, USA
[b] Department of Radiation Oncology, Vanderbilt-Ingram Cancer Center, Vanderbilt University Medical Center, Nashville, TN, USA
[c] Department of Neurology, Vanderbilt University Medical Center, Nashville, TN, USA
[d] Department of Psychiatry and Behavioral Sciences, Vanderbilt University Medical Center, Nashville, TN, USA
[e] Department of Electrical and Computer Engineering, Vanderbilt University, Nashville, TN, USA
[f] Department of Radiation Oncology, Harold C. Simmons Comprehensive Cancer Center, UT Southwestern Medical Center, Dallas, TX, USA

ARTICLE INFO

Keywords:
MRI
Magnetic resonance imaging
Tissue oxygenation
PET
Positron emission tomography
Hypoxia
Tumor hypoxia
Radiation
Adaptive radiation
Brain malignancy
Glioblastoma
Brain metastases

ABSTRACT

Tumor hypoxia indicates a worse prognosis in brain malignancies; however, current gold-standard methods for assessing tumor hypoxia are invasive and often inaccessible. Magnetic Resonance Imaging (MRI) is widely available, but its validity for identifying tumor hypoxia or hypoxia-related neoangiogenesis is not well characterized. A systematic literature search was performed across PubMed and Embase Databases. The search query identified MRI studies that validated hypoxia-surrogate imaging sequences against gold-standard hypoxia or neoangiogenesis detection methods in patients with brain malignancies. Literature screen identified 23 manuscripts published between 2007 and 2022. Among conventional MRI sequences, peritumoral edema and signal change after contrast administration were associated with gold-standard oxygen-assessment methods. T2*- and T2′-derived measures were associated with gold-standard methods, while reports on quantitative measures of oxygen extraction fraction were conflicting. Fiber density, tissue cellularity, blood volume, vascular transit time, and permeability measurements were associated with gold-standard methods, whereas blood flow measurements yielded conflicting results. MRI measures are promising surrogates for tumor hypoxia or hypoxia-related neoangiogenesis. Additional studies are needed to reconcile disparate findings. Future sensitivity analyses are needed to establish the MRI methods most accurate at identifying tumor hypoxia.

Introduction

Tissue hypoxia is defined as an arterial partial pressure of oxygen (pO_2) less than 10 mmHg [1]. Hypoxic conditions occur frequently in solid tumors [2] and are a consequence of rapid cell proliferation, with cellular tissue outgrowing the blood supply, resulting in inadequate oxygen delivery. Hypoxia during tumor development often triggers neoangiogenesis. However, tumor vasculature suffers from haphazard morphological organization, increased vascular fenestration and permeability due to downregulated connexin expression, and decreased stability due to pericyte disengagement from endothelial cells [3]. This dysfunctional tumor vasculature fails to meet the oxygen demand, further maintaining the hypoxic state [4]. Ultimately, oxygen delivery becomes insufficient for sustaining cellular functions, 'leading to cell death and the development of a poorly perfused necrotic tumor core [5].

Tumor hypoxia is known to drive malignant progression by modulating cellular responses, including oncogene activation [6], alteration of glucose and fat metabolism [7], promotion of genetic instability [8], and enhancement of ineffective neoangiogenesis [9]. Hypoxic tumors are also associated with a higher risk of developing distant metastases, which render many cancers incurable, and reduce the efficacy of local therapies [10]. Importantly, hypoxic tumors are more resistant to both radiation and chemotherapy. Hypoxia-induced radiation resistance occurs through multiple mechanisms, including reduced generation of reactive oxygen species (ROS) per unit radiation, as well as alterations in the tumor microenvironment that promote oxidative stress tolerance [11]. Collectively, these mechanisms result in reduced radiation-mediated cell death and apoptosis [12,13]. Hypoxia decreases the

* Corresponding author at: Department of Radiation Oncology, Harold C. Simmons Comprehensive Cancer Center, UT Southwestern Medical Center, 2280 Inwood Road, Dallas, TX 75235, United States.
E-mail address: jill.deVis@UTSouthwestern.edu (J.B. De Vis).

https://doi.org/10.1016/j.ctro.2025.100940
Received 17 October 2024; Received in revised form 17 February 2025; Accepted 25 February 2025
Available online 27 February 2025

efficacy of systemic therapies by impairing drug delivery [14], increasing drug efflux, and modulating immune responses [15]. As such, these factors make pretreatment tumor hypoxia one of the strongest prognostic indicators for unfavorable clinical outcomes [10].

Reliable assessment of tumor hypoxia, once available, would have important implications for the treatment of cancer patients. However, most radiotherapy treatments are currently prescribed using a "one-size fits all" strategy, independent of tumor microenvironmental conditions, where dose and fractionation are based solely on broad histological tumor subtyping. Accurate and clinically implementable tumor hypoxia assessments could instead allow for individualized tumor dosing, making it easier to escalate or de-escalate therapy based on the degree of tumor hypoxia detected. Furthermore, minimally-invasive and cost-effective hypoxia assessments can allow repeated measurements over time, permitting clinicians to make dynamic therapy adaptations in response to evolving microenvironmental tumor conditions. Recent work has preliminarily demonstrated the utility of adapting treatment to tumor hypoxia measured by positron emission tomography (PET) in head and neck cancers [16]. However, even though PET imaging is a minimally-invasive technique, the limited availability of hypoxia-sensitive radiotracers precludes large-scale implementation. Magnetic Resonance Imaging (MRI) sequences sensitive to tissue oxygenation may be more accessible while still providing a minimally invasive evaluation. However, as of now, it is unclear, which MRI sequence is most sensitive to tissue oxygenation. Therefore, in this review, we set out to systematically identify published literature comparing MRI findings to gold-standard oxygen assessment methods. Our search was focused on studies reporting data of patients with intracranial malignant disease, to remove organ-associated variability from our assessment.

Background

Current gold-standard methods to quantify tumor hypoxia include polarographic oxygen electrodes, immunohistochemistry (IHC) staining of hypoxia markers on tumor specimens, and PET imaging with hypoxia-sensitive radiotracers [10,17]. However, clinical implementation of these methods is limited due to their invasiveness, availability, and associated radiation exposure. MRI is a widely available imaging modality that can potentially evaluate tumor hypoxia without ionizing radiation in a non- or minimally-invasive manner. Below, we summarize gold-standard oxygen assessment methods and MRI sequences that have been evaluated as surrogate measures for brain tissue oxygenation.

Polarographic oxygen electrodes

Polarographic oxygen electrodes are probes that directly measure the pO2 in the tissue of interest. The electrodes assess tissue hypoxia by measuring the currents generated by oxygen, which is proportional to the level of pO2. Each electrode can measure the mean oxygen level of 50–100 cells neighboring the electrode [18]. This method is widely regarded as a gold-standard for tumor hypoxia assessment and often used to validate new techniques. However, probe insertion is invasive, can potentially damage the target tissue, and can introduce a source of infection in immunocompromised cancer patients, which collectively preclude frequent and repeated measurements [17].

Endogenous markers of hypoxia and neoangiogenesis

Hypoxia-induced changes in gene and protein expression can be sensitively quantified via tissue IHC staining, plasma protein assays, and RNA expression profiling. One of the most well-studied markers is hypoxia-inducible factor 1 alpha (HIF-1α), an oxygen-dependent transcriptional activator for various cellular pathways like neoangiogenesis and cell proliferation. HIF-1α protein is continuously expressed and degraded under normoxic conditions, but it accumulates in hypoxic tissues and it can be detected through various assays [19]. Hypoxia also induces the expression of carbonic anhydrase IX (CA-IX), which is an enzyme involved in adaptation to hypoxia-induced acidosis [20], as well as that of glucose transporter 1 (GLUT-1), which increases the efficiency of anaerobic metabolism in hypoxic tissue [21].

Neoangiogenesis, or the development of new vessels, is directly upregulated in response to hypoxia [22]. Vascular endothelial growth factor (VEGF) is a major upstream regulator of tumor neoangiogenesis [23] while endoglin (CD105) is a transmembrane glycoprotein primarily expressed in proliferating endothelial cells [24]. Tumor neoangiogenesis can also be assessed on hematoxylin and eosin stain (H&E) by pan-endothelial markers such as CD31, CD34, and factor VIII. Albeit not specific to proliferating endothelial cells, these markers can evaluate tumor neoangiogenesis by assessing vasculature density and morphology.

While IHC and other indirect tissue-based methods can evaluate hypoxia in surgically resected specimens, their clinically application is limited in patients who do not undergo surgery. Also, due to the heterogenous distribution of hypoxia across malignant tumors, application of these techniques to small sample biopsy specimens will not accurately represent the entirety of the tumor. For these reasons, non-invasive, image-based approaches is more preferrable.

Positron emission tomography

Hypoxia PET imaging requires injection of a hypoxia-sensitive radiolabeled tracer. After injection into the bloodstream, radiotracer molecules diffuse into viable cells and are then reduced. Reduced radiotracers are re-oxidized in normoxic tissues and diffuse out of the cell, but they are further reduced in hypoxic tissues, due to reductase upregulation in viable hypoxic cells [17]. Reduced radiotracers are trapped intracellularly [17]. As such, radiotracer uptake, and consequently emitted signal, is enhanced only in hypoxic regions, but not in normoxic or necrotic tissues [17].

Commonly used radiolabeled tracers for hypoxia PET imaging include 18F-FMISO, 18F-FAZA, 18F-FETNIM, 18F-HX4, 18F-EF5, 18F-EF3, 18F-FETA, 124I-IAZG, Cu-ATSM, 124I-cG250, and 89Zr-cG250-F(ab')$_2$ [25,26]. Uptake of these radiotracers has been shown to correlate with IHC staining for hypoxic markers [26–29], and the tracers have been used in studies evaluating tumor hypoxia in head and neck, esophageal, cervical and brain tumors [30]. In addition, radiotracer uptake has been used as an imaging strategy to guide radiation dose de-escalation in human papillomavirus-related oropharyngeal carcinoma [16]. To date, the radiotracers are considered investigational PET agents, which require an Investigational New Drug (IND) Exemption from the Food and Drug Administration (FDA) for use in clinical trials. In addition, production of most of these tracers requires an on-site cyclotron, which is not available in most centers.

Magnetic resonance imaging

Magnetic resonance imaging allows for visualization of tissue characteristics. The most used MRI sequences are T1- and T2-weighted scans. T1-weighted imaging is useful for visualizing anatomical details, while T2-weighted imaging is more sensitive to edema. T2-Fluid-attenuated inversion recovery (T2-FLAIR), T2*, and T2′ are variations of T2-weighted imaging where FLAIR is a T2-weighted image with suppression of cerebrospinal fluid signals, T2* detects local inhomogeneities in the magnetic field in addition to the T2 signal, and T2′ detects magnetic inhomogeneities only [30]. Due to the relationship between local field inhomogeneities and deoxyhemoglobin, T2* and T2′ methods have been considered surrogate measures for tissue deoxygenation, and have been used to calculate oxygen extraction fraction (OEF), which reflects the calculated ratio between the rate of oxygen consumption relative to that of oxygen delivery (Fig. 1) [31].

Diffusion-weighted imaging (DWI) captures proton mobility or diffusion. Diffusion Tensor imaging (DTI) extends from DWI and

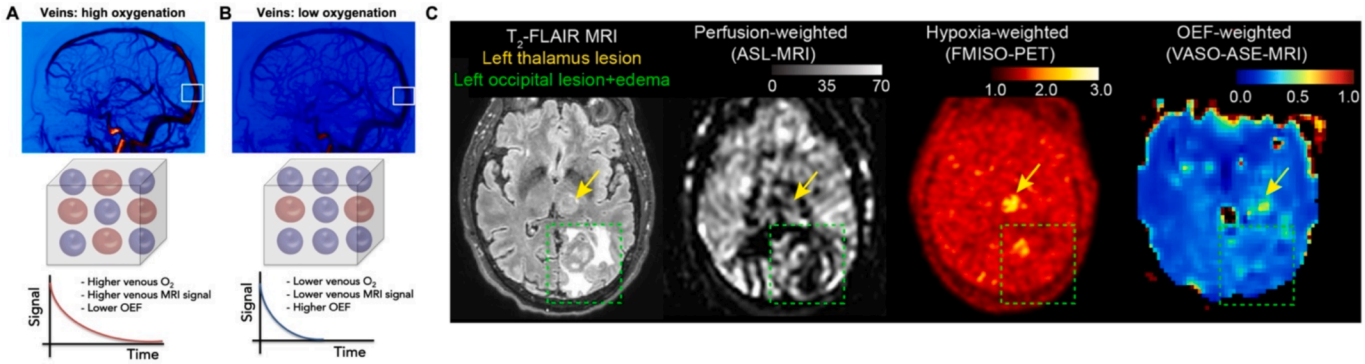

Fig. 1. Oxygenation imaging with magnetic resonance imaging (MRI). Blood oxygenation imaging with MRI generally exploits the principle that oxy-hemoglobin is diamagnetic (i.e., limited effect on surrounding water signal), whereas deoxy-hemoglobin is paramagnetic (i.e., attenuates surrounding water signal). The principle is shown schematically in (A-B), whereby higher venous oxygenation in the sagittal sinus, and corresponding lower oxygen extraction (OEF), leads to higher overall water signal and slower signal decay, whereas (B) lower venous oxygenation, and corresponding higher OEF, leads to lower signal and faster water signal decay. These effects can be assessed by measuring water decay within [74] or surrounding [75], the veins, and applying appropriate intravascular or extravascular signal models to convert the signal to blood oxygenation. (C) Example images obtained in our lab of a 63-year-old male patient with metastatic non-small cell lung cancer and a left thalamic lesion (yellow arrow) as well as a left occipital lesion with surrounding edema (green box). Both lesions yield similar perfusion-weighted signal, yet the thalamic lesion has evidence of hypoxia and high FMISO uptake on PET, and corresponding increased OEF on OEF-weighted vascular space occupancy asymmetric echo magnetic resonance imaging (VASO-ASE-MRI), which quantifies extravascular water signal and nearby venous oxygenation [76]. (For interpretation of the references to colour in this figure legend, the reader is referred to the web version of this article.)

measures both the directionality and magnitude of water diffusion. DWI-associated parameters are related to cellular density [32]; diffusion is more constricted in tissues with higher cellular density, which are more prone to developing tissue hypoxia due to higher oxygen demand [33].

Dynamic contrast-enhanced (DCE) and dynamic susceptibility contrast (DSC) [34] MRI assesses temporal changes in signal characteristics after administering a contrast agent. Whereas DCE detects the change in contrast concentration over time as an indicator of tissue vascularity, DSC measures the change in the tissue magnetic susceptibility as a reflection of tissue perfusion. DCE and DSC both measure properties related to contrast agent transit, such as capillary transit time, capillary transit time heterogeneity (CTTH), time to peak (TTP), and washout rate. Perfusion related measures can also be extracted from DCE and DSC, including blood volume, plasma volume, and blood flow. Contrary to DCE and DSC, Arterial Spin Labeling (ASL) assesses tissue perfusion without needing an exogeneous contrast agent. Instead, it magnetically labels arterial blood, which perfuses into tissue as an endogenous contrast agent (Fig. 2) [35].

Other than structural, physical, or functional properties, MRI can also assess the chemical composition of tissue. Magnetic Resonance Spectroscopy Imaging (MRSI), which acquires a spectral range, is a well-known example. The signal amplitudes at different frequencies are mapped to nuclei in various metabolites that resonate at different frequencies, facilitating assessment of the relative concentrations of different substances [36]. In Chemical Exchange Saturation Transfer (CEST) imaging, a radiofrequency pulse is applied at the resonance

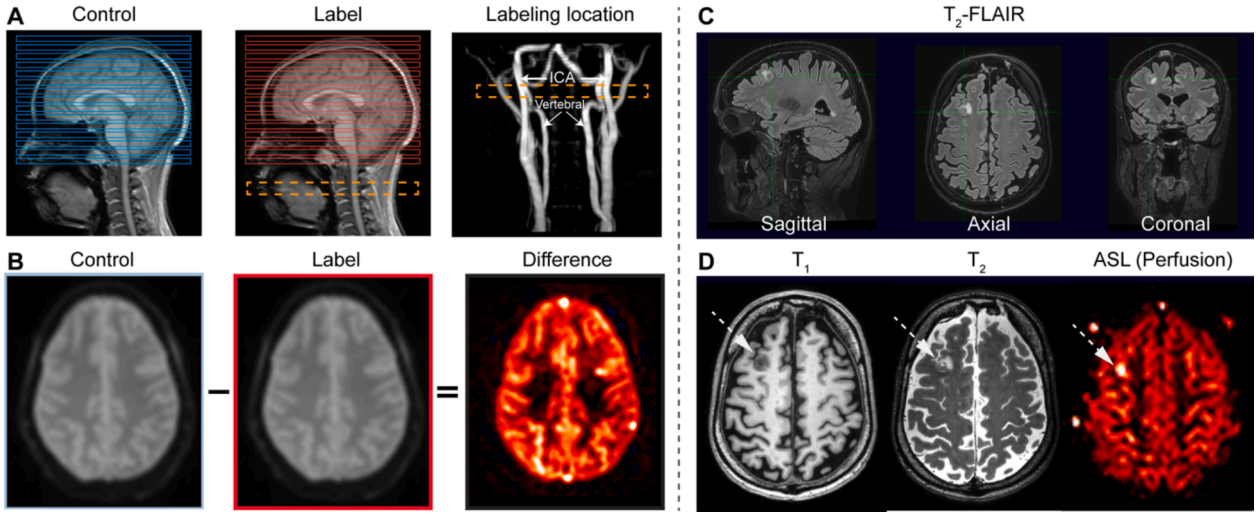

Fig. 2. Arterial spin labeling (ASL) magnetic resonance imaging for non-invasive perfusion quantification. (A) Sequential images without (e.g., control) and with (e.g., label) non-invasive radiofrequency labeling of blood water are acquired, with labeling frequently performed at the level of the cervical internal carotid arteries and vertebral arteries. Following labeling, a delay time is allowed during which the labeled blood water flows to the capillary exchange site, exchanges with tissue water, and attenuates the tissue water; the extent of the tissue water attenuation reflects the amount of blood water delivery, or perfusion. (B) The perfusion can be quantified in units of ml blood / 100 g tissue / minute by subtracting the label image from the control image and upon application of the solution to the flow-modified Bloch equation. To the right, example images obtained in our lab of a 61-year-old male patient with a right frontal metastasis secondary to melanoma; orthogonal 3D T2-FLAIR images are shown above (C) and corresponding axial (D) T_1, T_2, and perfusion-weighted ASL images are shown below, whereby the white arrow identifies the hyperperfused lesion. The ASL method requires approximately 3–5 min and can be obtained with a spatial resolution of 3–5 mm per voxel dimension and is analogous to bolus tracking with gadolinium-MRI but can be applied more readily for surveillance or when exogenous contrast agents are contraindicated [35].

frequency of a chemical species of interest, after which the magnetization is transferred to water molecules, allowing observation of the saturation effect on water. Amide Proton Transfer CEST (APT-CEST) is the best-known example of this technique, where the magnetization is transferred between amide and water protons, and the image contrast scales directly with the local protein content and inversely with tissue pH (Fig. 3) [37].

Method

Search strategy

The authors consulted with a medical librarian to identify the appropriate MeSH terminology and key words for the PubMed search strategy, which is translated to Embase (via Ovid). The search strategy was designed to retrieve papers that (1) validated MRI parameters to gold-standard tumor or tissue hypoxia/neoangiogenesis methods as described above, and/or (2) evaluated the association between MRI-derived measures and patients' outcome both in terms of tumor control and complication probability. In short, index terms and keywords were retrieved for the following three components: (1) MRI, MRI sequences and MRI parameters, (2) malignant intracranial disease, (3) tumor hypoxia OR disease outcome. The database search was performed on PubMed and Embase on June 24th, 2024. The full search strategy is available in the supplementary material. This paper reports on search results associated with our first research question as outlined above.

Selection criteria

This review paper reports on literature results related to our first research question, i.e. studies that validated MRI parameters to gold-standard tumor or tissue hypoxia/neoangiogenesis. Studies eligible for inclusion were original research studies reporting on in-vivo human-subject data from patients with intracranial malignant disease. Acceptable gold-standard techniques included polarographic oxygen electrodes, histopathology staining of biopsy tissue for hypoxia or neoangiogenesis related markers (HIF1α, CA-IX, VEGF, CD31, CD34, factor VIII, and vasculature density on H&E), and PET with hypoxia tracers (18F-FMISO, 18F-FAZA, 18F-HX4, 18F-FETNIM, and Cu-ATSM). Study participants had to undergo both MRI and a gold-standard technique for measuring tissue oxygenation, and parameters obtained by the two techniques had to be directly compared. Only studies with five or more subjects were included. There were no limits regarding tumor type or treatment status. Both prospective and retrospective study designs were allowed. Case reports, abstracts, systematic reviews, letters, comments, and overview articles were excluded. Studies written in languages other than English, French, Dutch, or German were excluded. There was no restriction on the publication year.

Study selection and data extraction

Identified articles were imported to Covidence for deduplication, study selection, and data extraction (Covidence systematic review software, Veritas Health Innovation, Melbourne, Australia. Available at www.covidence.org). Two independent reviewers (YB, JDV) screened title and abstracts according to the predefined selection criteria. Both reviewers met regularly to discuss and resolve discrepancies. Full text review was performed by the two reviewers using the same process.

Data extraction was performed using a standardized data extraction form. Extracted information included general paper information, patient tumor type and demographics, MRI sequences and parameters, hypoxia gold-standard technique, and textual and statistical characterizations of the relationship between MRI and validation technique parameters. One reviewer (YB) performed the data extraction, and the extracted data was checked by another independent reviewer (JDV).

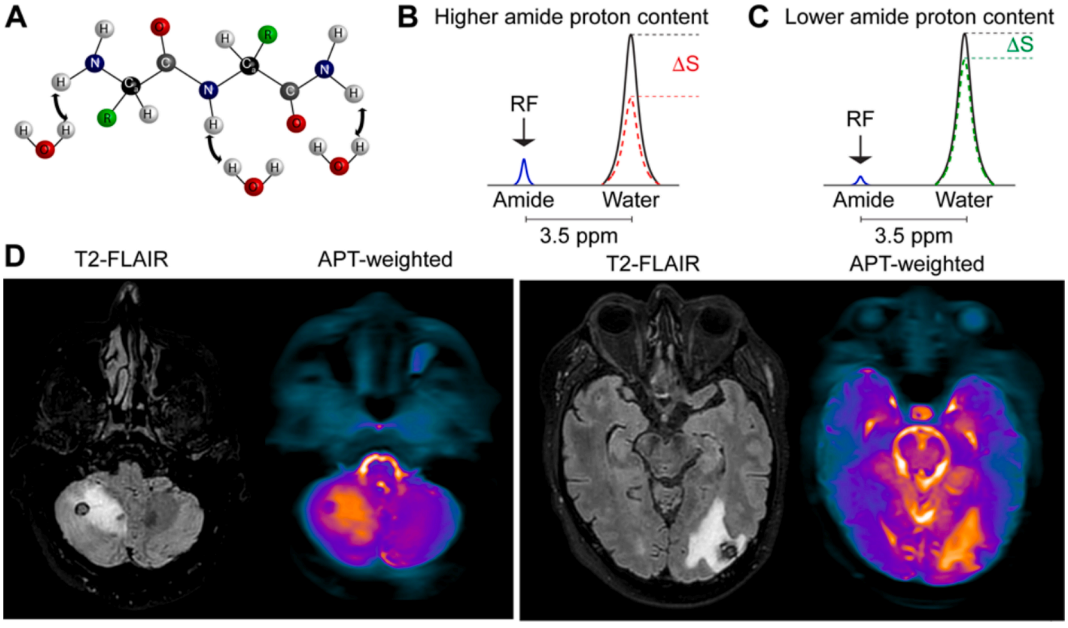

Fig. 3. Chemical exchange saturation transfer (CEST) magnetic resonance imaging (MRI). Like other MRI contrasts, CEST MRI measures water signal, however, exploits the physical property that many proton moieties, such as amide protons on the peptide backbone as shown in (A), are in constant exchange with water. As different protons resonate (e.g., absorb radiofrequency, RF, energy) with discrete and unique energies, it is possible to apply RF energy at the resonance of the exchanging proton, and subsequently allow time for the proton to exchange with surrounding water protons. Amide protons resonate at approximately 3.5 parts per million (ppm) from the water resonance. The degree of attenuation in the water signal with vs. without the RF pre-pulse can be used to estimate the exchanging proton concentration (B-C), and, as effects are base-catalyzed over a physiological range, pH. (D) Example images obtained in our lab of a 61-year-old male with metastatic renal cell carcinoma and right cerebellar and left occipital lesions, each with a hemorrhagic core and surrounding edema. The amide proton transfer (APT)-weighted images, which are proportional to the protein content, show low protein content in the hemorrhagic core and high content in the surrounding edema and tumor margins [37].

Results

PubMed and Embase search identified 14,787 studies, of which 3986 duplicates were removed. Hereafter, 10,801 studies remained for title and abstract screen where consensus read found 10,584 irrelevant for our prespecified first research question, and 217 articles proceeded to full-text screen. Of these 217 articles, 171 articles were excluded due to either being a conference abstract or because full text was unavailable, 1 article was excluded due to wrong article format, and 21 studies did not follow the outlined study design or format. Ultimately, 24 studies remained for data extraction [32,38–60] (Fig. 4).

Studies were published from 2007 to 2024. The median number of subjects in the 24 studies was 29, and the range was between 7 and 203 subjects. Nearly all (23 out of 24) studies enrolled patients with glioma [32,38–52,54–60], with 12 studies limiting inclusion to grade 4 glioma [32,38–41,43,47–50,54,55], and 3 studies extending the inclusion criteria to either meningioma, lymphoma and/or germinoma in addition to glioma [42,44,51]. Two studies enrolled patients with brain metastases [53,59]. Nine studies evaluated the utility of conventional imaging to detect tumor hypoxia/neoangiogenesis [38,43,46,47,49,52–55], 5 studies utilized diffusion weighted techniques [32,38,42,49,52], 10 studies used perfusion-weighted techniques with an exogeneous tracer, 1 study used blood labeling as an endogenous tracer, and 6 studies used more advanced functional or quantitative MRI techniques. Gold-standard methods were IHC in 11 papers [32,38,44–46,52,53,56–59], H&E in 2 papers [46,60], and PET with a nitroimidazole-derivative tracer in 10 papers [41–43,47–51,54,55]. Immunoassay [44] and oxygen electrode [45] were both used in 1 paper, and gene expression profile was used in 2 papers [39,40] (Table 1).

Measurements derived from conventional MRI sequences

Twenty papers included conventional imaging in their study methods, but only 9 papers investigated the validity of measurements derived from T1-weighted, T2-weighted, and T2-FLAIR MRI sequences as a surrogate for tissue hypoxia or neoangiogenesis [38,43,46,47,49,52–55] (Table 2). The most studied volumes of interest (VOI) include contrast-enhancing (CE) tumor (contrast-enhancing T1 hyperintensity), non-enhancing (NE) tumor (non-enhancing T1 hyperintensity inside CE tumor), and peritumor edema (defined on T2-weighted images). The difference between pre- and post-contrast T1 signal intensity was examined by 3 papers [38,46,52]. Of these 3 papers, a positive correlation with factor VIII and HIF-1α in the CE tumor region was reported by Barajas et al. [38] ($p = 0.027$ with factor VIII) and Shu et al. [52] ($r = 0.431$, $p = 0.012$ with HIF-1α). In contrast, Maurer et al. did not find a significant relation with CA-IX [46]. Other T1-weighted measurements positively associated with gold-standard measures included CE volume [47], CE surface area [54], T1 signal strength [49], and the volume ratio between CE and peritumoral edema [43]. Post-contrast T1 relaxation time [46], and post-contrast T1 CE sphericity [55] were negatively associated with gold-standard.

Five papers studied properties related to peritumoral edema [38,43,52–54] using T2-weighted sequences. Spangerber et al. reported a positive association for the extent of peritumoral edema with HIF-1α ($p = 0.04$) and with H&E microvascular density ($p = 0.01$) [53], but Shu et al. reported an insignificant relationship between this property and HIF-1α [52]. Swanson et al. found a positive association for peritumoral edema surface area measured on T2 with hypoxic volume surface area on 18F-FMISO PET ($r = 0.78$, $p = 0.005$), but no significant correlation was found for peritumoral edema volume [54]. On the other hand, no significant correlation was found for T2-FLAIR signal strength or T2-FLAIR volume with hypoxia gold-standard measures in studies by Huang et al. and Barajas et al. [38,43] T2 relaxation time [46] and T2 CE sphericity [55] negatively correlates with gold-standard. All other conventional-MRI-derived measurements were only investigated by single studies [43,46,47,49,52,54,55].

Tissue hypoxia related MRI measures

Results of tissue hypoxia-related MRI measures are shown in Table 3. Three papers reported on T2*, T2′ or R2′ (inverse of T2′) imaging sequences [46,48,58]. Significant associations were found in 2 of 3 papers with an inverse relation between T2* and T2′ with vessel density [46] ($r = -0.235$ and -0.264, respectively), and a positive correlation for R2′ with HIF-1α expression [58] ($r = 0.667$), which is consistent with the inverse correlation for T2* and T2′.

Three studies evaluated how T2*-derived OEF was related to surrogate measures of hypoxia [48,56,59]. Toth et al. used OEF to stratify regions of varying HIF-1α expression strength, achieving a sensitivity of 0.50 and specificity of 0.71 on 6 patients who underwent image-guided

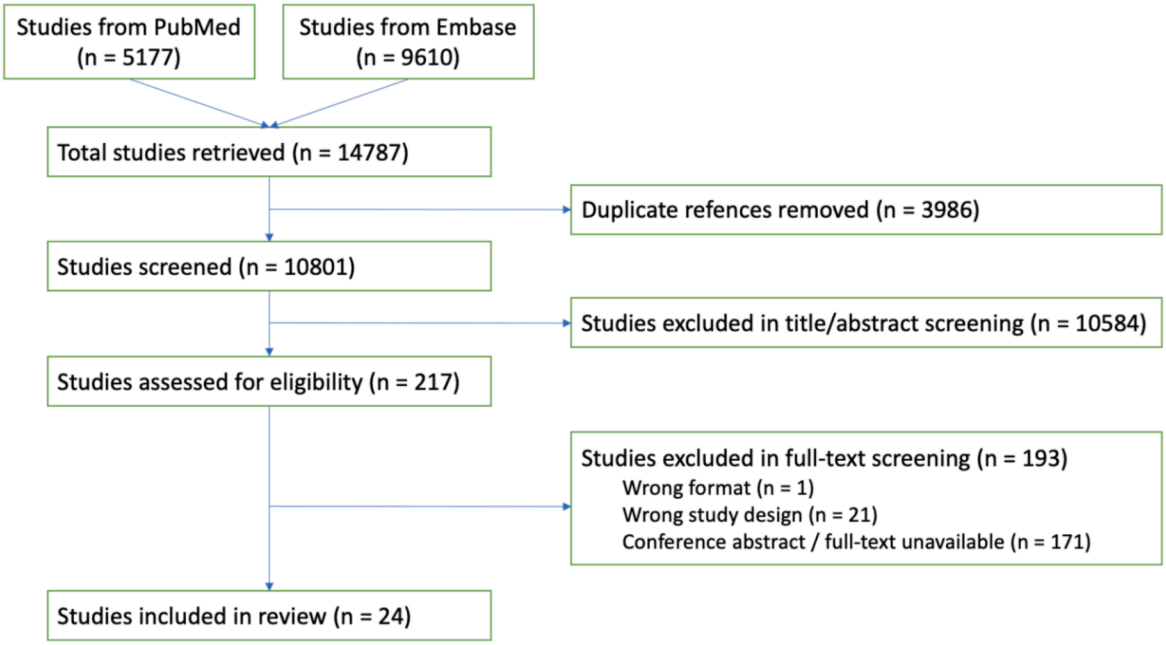

Fig. 4. PRISMA flow diagram summarizing the literature screening process.

Table 1
Baseline characteristics of included studies.

Authors	Publication year	# subjects	Tumor histology	MRI sequence	Gold-standard method
Sadeghi et al.[60]	2007	7	Glioma	CI, DSC	H&E: Endothelial cell proliferation
Barajas Jr et al.[38]	2012	51 (35)*	GBM	CI, DWI, and DSC	IHC: CA-IX, factor VIII
Barajas Jr et al.[32]	2013	18	GBM	CI, DWI	IHC: CA-IX, factor VIII
Spanberger et al.[53]	2013	129	Brain metastasis	CI	IHC: HIF-1α, CD34
Toth et al.[56]	2013	34 (6)**	Glioma	qMRI	IHC: HIF-1α
Jensen et al.[44]	2014	18	Glioma, meningioma	DCE	IHC: HIF-1α, CA-IX, factor VIII, VEGF Immunoassay: HIF-1α, VEGF
Shu et al.[52]	2016	33	Glioma	CI, DWI	IHC: HIF-1α
Maralani et al.[45]	2018	10 (9)**	Glioma	CI, qMRI	IHC: HIF-1α, CA-IX, VEGF, CD105 Oxygen electrode: pO_2
Xie et al.[57]	2018	34	Glioma	CI, DCE	IHC: HIF-1α
Yao et al.[58]	2019	90 (20)**	Glioma	CEST-SAGE-EPI	IHC: HIF-1α
Maurer et al.[46]	2021	25	Glioma	CI, qMRI	IHC: CA-IX H&E: vessel density
Arzanforoosh et al.[59]	2023	10	Glioma, brain metastasis	CI, FLAIR-ASE, DSC, DWI	IHC: HIF-1α, CD31
Swanson et al.[54]	2009	29	GBM	CI	18F-FMISO PET
Szeto et al.[55]	2009	11	GBM	CI	18F-FMISO PET
Shishikura et al.[42]	2014	34	Glioma, lymphoma	CI, DWI	62Cu-ATSM-PET
Gerstner et al.[41]	2016	50	GBM	CI, DCE, DSC	18F-FMISO PET
Ferreira da Ponte et al.[47]	2017	23	GBM	CI, DSC, qMRI	18F-FMISO PET
Preibisch et al.[48]	2017	12	GBM	CI, DSC, qMRI	18F-FMISO PET
Ratai et al.[50]	2017	17	GBM	CI, MRSI	18F-FMISO PET
Shimizu et al.[51]	2020	15	GBM, lymphoma, germinoma	CI, DCE, ASL	18F-FMISO PET
Huang et al.[43]	2021	33	GBM	CI, DSC	18F-FMISO PET
Qin et al.[49]	2022	28	GBM	CI, DSC, DCE, DTI	18F-FMISO PET
Beig et al.[39]	2018	115	GBM	CI	Gene expression profile
Beig et al.[40]	2020	203	GBM	CI	Gene expression profile

ASL, arterial spin labeling; CA-IX, carbonic anhydrase IX; CEST-SAGE-EPI, chemical exchange saturation transfer spin- and-gradient echo echo-planar imaging; CI, conventional Imaging; DCE, dynamic contrast-enhanced; DSC, dynamic susceptibility contrast; DTI, diffusion tensor imaging; GBM, glioblastoma multiforme; GE, gradient echo; GRASE, gradient and spin Echo; H&E, hematoxylin and eosin staining; HIF1-α, hypoxia inducible factor 1 subunit alpha; IHC, immunohistochemistry; MRI, magnetic resonance imaging; MRSI, magnetic resonance spectroscopy imaging; qMRI, quantitative MRI; VEGF, vascular endothelial growth factor; 18F-FMISO PET, 18F-fluoromisonidazole positron emission tomography; 62Cu-ATSM-PET, 62Cu-diacetyl-bis(N4-methylthiosemicarbazone) positron emission tomography.
* The number in between brackets is the number of subjects in whom DSC imaging was obtained.
**The number in between brackets is the number of subjects that received image-guided biopsy, and it is this number of subjects that was used for data analyses.
*** The number in between brackets is the number of subjects in whom positron emission tomography (PET) imaging was obtained.
Table summarizing the baseline characteristics of studies selected for data extraction and analysis.

biopsy [56]. Preibisch et al. similarly found a moderate negative correlation for OEF with 18F-FMISO uptake ($r = -0.683$) when analyzing CE tumor and peritumoral edema regions together [48]. When VOIs were analyzed separately, both CE tumor and peritumoral edema exhibited a positive relationship between elevated OEF and CA-IX and CD31, though the strength of this finding was limited by its small sample size ($n = 12$) [48]. Arzanforoosh et al. did not find a statistically significant correlation between OEF and IHC HIF-1α [59].

One study assessed the value of T2*-derived oxygen saturation maps through a validation with IHC CA-IX and VEGF, and oxygen electrode pO2 measurements [45]. Results were promising but suffered from inter-reader variability on pathology read ($p = 0.03$ and $p = 0.28$). Yao et al. employed CEST to measure magnetization transfer ratio asymmetry (MTR_{asym}), a measurement related to tissue pH. They reported a positive correlation for MTR_{asym} with HIF-1α ($r = 0.610$, $p = 0.03$) [58]. Ratai et al. compared measurements derived from magnetic resonance spectroscopic imaging (MRSI) against those from 18F-FMISO PET [50]. No significant association was found.

Fiber density and tissue cellularity measurements

Five studies reported on the relationship between DWI or DTI [32,38,42,49,52] and tumor hypoxia (Table 4). Generally, significant associations were found for track density map intensity, apparent diffusion coefficient (ADC), and fractional anisotropy related to the CE tumor, NE tumor, and tumor and surrounding edema analyses [32,38,42,49,52]. Barajas et al. employed DWI to generate super-resolution track density mapping, which is thought to represent the combined effects of fiber disruption, edema, microscopic hemorrhage, and necrosis. When analyzing CE and NE regions separately as well as combined, they reported a positive relation for track density mapping intensity with CA-IX and factor VIII [32]. Analyzing CE and NE regions separately, two studies found a strong negative association between ADC and HIF-1α ($r = -0.756$) [52] or 62Cu-ATSM PET ($r = -0.532$) [42]. However, ADC exhibited a weak positive correlation with 18F-FMISO PET when analyzing tumor and edema in its entirety ($r = 0.183$) [49]. ADC and fractional anisotropy did not show a significant association with IHC factor VIII when analyzing the tumor in its entirety (CE + NE) [32].

Measures of neoangiogenesis and vascular bed transit times

Blood volume (BV), blood flow (BF), extraction fraction (EF), and vessel size MRI measures were assessed as surrogates for tumor hypoxia induced neoangiogenesis in 9 papers [38,43,44,47–49,57,59,60]. Measurements of BV were mostly significantly associated with tissue hypoxia or neoangiogenesis gold-standard measures [38,44,47,49,60] except for data published by Xie et al, Huang et al, Preibisch et al., and Arzanforoosh et al (Table 5) [43,48,57,59]. The highest correlation coefficient ($r = 0.77$) was found by Ponte et al., who validated BV measurements against tumor hypoxia detected by 18F-FMISO PET [47]. Half of the papers reporting on BF measurements found no significant relation [43,44,48,57], while the other half did (Table 5) [38,47,48,60]. Jensen et al. also found a strong positive correlation between extraction fraction (EF) and HIF-1α in the NE region ($r = 0.943$, $p = 0.017$) [44]. Arzanforoosh et al. reported a positive correlation between vessel diameter measured by CD31 and vessel size ($r = 0.67$, $p < 0.001$), with the latter being computed from CBV and ADC values [59].

Table 2
Measurements derived from conventional sequences.

VOI	Authors	# subjects	Gold-standard	Correlation
Tumor volume				
CE	Swanson et al. [54]	29 (11)*	18F-FMISO PET	p = 0.006, r = 0.762
	Ponte et al. [47]	23	18F-FMISO PET	p < 0.001, r = 0.91
Tumor surface area				
CE	Swanson et al. [54]	29 (11)*	18F-FMISO PET	p = 0.0002, r = 0.900
Tumor sphericity				
CE	Szeto et al. [55]	11	18F-FMISO PET	p < 0.02 (T1Gd) p < 0.05 (T2)
Edema volume				
Edema	Spanberger et al.[53]	129	IHC: HIF-1α	p = 0.04
			IHC: CD34 vessel density	p = 0.03
	Shu et al.[52]	33	IHC: HIF-1α	p > 0.05
	Swanson et al. [54]	29 (11)*	18F-FMISO PET	ns
	Huang et al. [43]	33	18F-FMISO PET	ns
Edema surface area				
Edema	Swanson et al. [54]	29 (11)*	18F-FMISO PET	p = 0.005, r = 0.781
Tumor-edema volume ratio				
Tumor and edema	Huang et al. [43]	33	18F-FMISO PET	p < 0.001, r = 0.69
MRI signal intensity				
CE	Shu et al.[52]	33	IHC: HIF-1α	p < 0.001, r = 0.661 (T1Gd)
Tumor and edema	Qin et al.[49]	28	18F-FMISO PET	p < 0.001, r = 0.178 (T1Gd)
Edema	Barajas et al. [38]	51 (35) **	IHC: factor VIII	ns (FLAIR)
Relaxation time				
CE	Maurer et al. [46]	25	H&E: vessel density	p < 0.001, r = -0.248
			IHC: CA-IX	p = 0.004, r = -0.191 (T1Gd) p = 0.002, r = -0.200 (T2)
Difference between pre- and post-contrast T1 signal intensity				
CE	Barajas et al. [38]	51 (35) **	IHC: factor VIII	p = 0.027
	Shu et al.[52]	33	IHC: HIF-1α	p = 0.012, r = 0.431
	Maurer et al. [46]	25	IHC: CA-IX; H&E: vessel density	ns

CE, contrast-enhancing portion of the tumor; HIF1-α, hypoxia inducible factor 1 subunit alpha; IHC, immunohistochemistry; NE, non-contrast-enhancing portion of the tumor; VEGF, vascular endothelial growth factor; VOI, volume-of-interest; 18F-fluoromisonidazole positron emission tomography.
* The number in between brackets is the number of subjects in the pre-operative group, in which this specific finding applies.
** The number in between brackets is the number of subjects in whom DSC imaging was obtained, and it is this number was used for data analyses.
Table summarizing data on measurements derived from conventional MRI sequences. Authors reported on data obtained from the contrast-enhancing portion of the tumor (CE), the non-contrast-enhancing portion of the tumor (NE), the entire tumor (CE + NE), or the tumor with surrounding edema. Gold standard methods used for comparison are shown.

Five papers reported on vascular bed transit time related measures [38,43,44,49,57] (Table 6). When CE and peritumoral edema regions were analyzed separately, three papers reported that gold-standard measures correlates with longer transit time-related measures except for washout rate (Table 6) [38,44,57]. The highest correlation coefficients were found between longer capillary transit time and HIF-1α in CE (r = 0.659) [44], and between higher capillary heterogeneity and

Table 3
Tissue hypoxia related measures.

VOI	Authors	# subjects	Gold-standard	Correlation
T2, T2′ or R2′*				
CE	Maurer et al. [46]	25	H&E: vessel density	p < 0.001, r = -0.235 (T2*)
CE	Maurer et al. [46]	25	H&E: vessel density	p < 0.001, r = -0.264 (T2′)
Tumor and edema	Yao et al.[58]	90 (20)*	IHC: HIF-1α	p = 0.008, r = 0.667 (R2′)
	Preibisch et al. [48]	12	18F-FMISO PET	ns
Relative Oxygen Extraction Fraction				
CE	Toth et al.[56]	34 (6)*	IHC: HIF-1α	Spe = 0.9
	Preibisch et al. [48]	12	IHC: CA-IX, CD31+	66.7 % CA-IX + and CD31 + in rOEF+ 50 % CA-IX+, 25 % CD31 + in rOEF-
NE	Toth et al.[56]	34 (6)	IHC: HIF-1α	Spe = 0.67
Tumor	Toth et al.[56]	34 (6)	IHC: HIF-1α	Spe = 0.71, sen = 0.5
Tumor and edema	Preibisch et al. [48]	12	18F-FMISO PET	p = 0.000, r = -0.683
Edema	Preibisch et al. [48]	12	IHC: CA-IX, CD31+	50 % CA-IX+, 75 % CD31 + in rOEF+ 0 % CA-IX+, 50 % CD31 + in rOEF-
Tumor and necrosis	Arzanforoosh et al.[59]	10	IHC: HIF-1α	p = 0.40
Tissue Oxygen saturation				
Tumor	Maralani et al. [45]	10 (9)*	IHC: VEGF	p = 0.03 and p = 0.28
			Oxygen electrode: pO2	p = 0.01, r = 0.73

CE, contrast-enhancing portion of the tumor; CA-IX, carbonic anhydrase IX; H&E, hematoxylin and eosin; IHC, immunohistochemistry; NE, non-contrast-enhancing portion of the tumor; spe, specificity; rOEF, relative oxygen extraction fraction; sen, sensitivity; VEGF, vascular endothelial growth factor; VOI, volume-of-interest; 18F-FMISO PET, 18F-fluoromisonidazole positron emission tomography.
*The number in between brackets is the number of subjects that received image-guided biopsy, and it is this number of subjects that was used for data analyses.
Table summarizing data on tissue hypoxia related MRI measures. Authors reported on data obtained from the contrast-enhancing portion of the tumor (CE), the non-contrast-enhancing portion of the tumor (NE), the entire tumor (CE + NE), or the tumor with surrounding edema. Gold standard methods used for comparison are shown. There are 2p values shown for the paper by Maralani et al., these are derived from ratings performed by two different pathologists. Overall, results of hypoxia related measures are variable with some finding a significant correlation while others (underlined) did not.

VEGF in peritumoral edema (r = 0.973) [44]. Qin et al. analyzed tumor and edema in its entirety and reported either weak or no significant relations between transit time related measures and gold-standard measures [49]. NE exhibited a strong positive correlation (r = 0.931) between washout rate and VEGF, reported by Jensen et al [44].

Permeability related MRI measures, including transfer constant, permeability-surface area product, and interstitial volume, were assessed in 3 papers [44,49,57] (Supplementary table). Positive associations were reported in 2 papers for transfer constant and interstitial volume with tissue hypoxia gold-standard measures [49,57], with transfer constant exhibiting the highest correlation coefficient (r = 0.686, p < 0.001) with HIF-1α in CE [57]. Jensen et al. found no

Table 4
Fiber density and tissue cellularity measurements.

VOI	Authors	# subjects	Gold-standard	Correlation
Track density				
CE	Barajas et al. 2013[32]	18	IHC: CA-IX	$p = 0.01$
			IHC: factor VIII	$p = 0.02$
NE	Barajas et al. 2013[32]	18	IHC: CA-IX	$p = 0.02$
Tumor	Barajas et al. 2013[32]	18	IHC: CA-IX	$p = 0.01$, OR = 3.52
			IHC: factor VIII	$p = 0.02$
Apparent diffusion coefficient				
CE	Shu et al.[52]	33	IHC: HIF-1α	$p < 0.001$, $r = -0.756$
	Shishikura et al. [42]	34	62Cu-ATSM PET	$p < 0.0001$, $r = -0.532$
Tumor	Barajas et al. 2013[32]	18	IHC: factor VIII	$p = 0.05$, OR = 0.28
Tumor and edema	Qin et al.[49]	28	18F-FMISO PET	$p < 0.001$, $r = 0.183$
Fractional anisotropy				
NE	Barajas et al. 2012[38]	51	IHC: factor VIII	$p = 0.009$
Tumor	Barajas et al. 2013[32]	18	IHC: CA-IX, factor VIII	$p > 0.08$
Tumor and edema	Qin et al.[49]	28	18F-FMISO PET	$p < 0.001$, $r = 0.082$

CE, contrast-enhancing portion of the tumor; CA-IX, carbonic anhydrase IX; HIF1-α, hypoxia inducible factor 1 subunit alpha; IHC, immunohistochemistry; NE, non-contrast-enhancing portion of the tumor; OR, odds ratio; VOI, volume-of-interest; 18F-FMISO PET, 18F-fluoromisonidazole positron emission tomography; 62Cu-ATSM PET, 62Cu-diacetyl-bis(N4-methylthiosemicarbazone) positron emission tomography.
Table summarizing data on fiber and tissue cellularity measurements obtained from diffusion tensor and diffusion weighted imaging. Authors reported on data obtained from the contrast-enhancing portion of the tumor (CE), the non-contrast-enhancing portion of the tumor (NE), the entire tumor (CE + NE), or the tumor with surrounding edema. Gold standard methods used for comparison are shown. Only T/B ratio values were reported for studies using PET validation methods. Most studies found significant correlations between fiber density or tissue cellularity measurements and tumor hypoxia as assessed by gold standard method. Non-significant correlations are underlined.

significant relation between any permeability measure and HIF-1α or VEGF [44].

MRI-derived radiomics and computational analysis

Five studies investigated the validity of tissue hypoxia assessments derived from computational MRI analyses [38–40,51,55]. Barajas et al. [38] developed two pairwise prediction models to predict factor VIII expression, including T1 with BV (odds ratio = 1.88, $p = 0.007$), and T1 with peak height (odds ratio = 2.43, $p = 0.002$). Shimizu et al. [51] developed a multivariate prediction model to predict 18F-FMISO PET mapping using arterial spin labeling, transfer constant, and perfusion volume, achieving an area under the curve (AUC) of 0.844 across 15 subjects.

Beig et al. [39,40] performed radiomics textural analyses on post-contrast T1, T2, and T2-FLAIR sequences. In their 2018 paper, 8 radiomic features were identified that most highly suggested the expression of hypoxia-associated genes [39]. In their subsequent 2020 paper, they developed a radiogenomics risk score (RRS) consisting of 25 radiomic features, O-6-methylguanine-DNA methyltransferase (MGMT) and isocitrate dehydrogenase (IDH) status, and clinical parameters [40]. The RRS was associated with the expression of genes involved in 13 neoangiogenesis pathways.

Szeto et al. [55] developed a biomathematical model to calculate tumor net proliferation, net diffusion, and aggressiveness using post-contrast T1 and T2 sequences. Both net proliferation and aggressiveness were positively associated with 18F-FMISO PET ($r = 0.911$ and $p < 0.001$, $r = 0.860$ and $p < 0.001$, respectively). No significant correlation was found with net diffusion.

Table 5
Blood volume and flow related measures.

VOI	Authors	# subjects	Gold-standard	Correlation
Blood/Plasma volume (DSC or DCE)				
CE	Barajas et al. [38]	51 (35)*	IHC: factor VIII	$p = 0.005$
	Jensen et al. [44]**	18	IHC: HIF-1α	$p = 0.043$, $r = 0.747$
			IHC: VEGF	$p = 0.032$, $r = 0.604$
	Xie et al.[57]	34	IHC: HIF-1α	$p = 0.219$, $r = 0.149$
Tumor	Sadeghi et al. [77]	14	H&E: endothelial cell proliferation	$p < 0.01$
	Ponte et al.[47]	23	18F-FMISO PET	$p < 0.001$, $r = 0.77$
Tumor and edema	Huang et al. [43]	33	18F-FMISO PET	$p = 0.01$, $r = 0.46$
	Ponte et al. [47]	23	18F-FMISO PET	$p = 0.002$, $r = 0.61$
	Qin et al.[49]	28	18F-FMISO PET	$p < 0.001$, $r = 0.418$ (CBV)
				$p < 0.001$, $r = 0.268$ (FPV)
	Huang et al. [43,49]	33	18F-FMISO PET	ns
	Preibisch et al. [48]	12	18F-FMISO PET	ns
Tumor and necrosis	Arzanforoosh et al. [59]	10	IHC: CD31	$p = 0.15$
Vessel size (DSC)				
Tumor and necrosis	Arzanforoosh et al. [59]	10	IHC: CD31	$p < 0.001$, $r = 0.67$
Blood flow (DCE)				
CE	Jensen et al. [44] **	18	IHC: HIF-1α, VEGF	$p > 0.05$
NE	Jensen et al. [44]	18	IHC: HIF-1α, VEGF	$p > 0.05$
Tumor and edema	Qin et al. [49]	28	18F-FMISO PET	$p < 0.001$, $r = 0.35$
	Preibisch et al. [48]	12	18F-FMISO PET	$p = 0.000$, $r = 0.674$
	Huang et al. [43]	33	18F-FMISO PET	ns

CE, contrast-enhancing portion of the tumor; CBV, cerebral blood flow; FPV, fractional plasma volume; HIF1-α, hypoxia inducible factor 1 subunit alpha; H&E, hematoxylin and eosin; IHC, immunohistochemistry; NE, non-contrast-enhancing portion of the tumor; VEGF, vascular endothelial growth factor; VOI, volume-of-interest; 18F-FMISO PET, 18F-fluoromisonidazole positron emission tomography.
* The number in between brackets is the number of subjects in whom DSC imaging was obtained, and it is this number was used for data analyses.
** Jensen et al further divided the contrast-enhancing VOI into an active tumor VOI and a hypoxic penumbra VOI, which is defined as the contrast-enhancing region surrounding the central necrosis. Findings were reported separately. This table lists findings from the active tumor VOI under the CE VOI.
Table summarizing data on blood/plasma volume and flow measurements. Authors reported on data obtained from the contrast-enhancing portion of the tumor (CE), the non-contrast-enhancing portion of the tumor (NE), the entire tumor (CE + NE), or the tumor with surrounding edema. Gold standard methods used for comparison are shown. In general, most studies evaluating blood or plasma volume measures as a surrogate for tumor hypoxia, found this measure to have a significant correlation. Blood flow or perfusion measurements on the other hand were mostly non-significant (underlined).

Table 6
Transit time related measurements.

VOI	Authors	# subjects	Gold-standard	Correlation
Washout rate (DCE)				
CE	Xie et al. [57]	34	IHC: HIF-1α	p = 0.072, r = 0.216
	Jensen et al. [44]**	18	IHC: HIF-1α, VEGF	p > 0.05
NE	Jensen et al. [44]	18	IHC: VEGF	p = 0.007, r = 0.931
Tumor and edema	Qin et al. [49]	28	18F-FMISO PET	p = 0.35, r = -0.002
Edema	Jensen et al. [44]	18	IHC: VEGF	p = 0.0065, r = 0.761
AUC (DCE)				
Tumor and edema	Qin et al. [49]	28	18F-FMISO PET	p < 0.001, r = 0.183
Capillary transit time (DCE)				
CE	Jensen et al. [44]**	18	IHC: HIF-1α	p = 0.017, r = 0.659
			IHC: VEGF	p = 0.034, r = 0.588
Edema	Jensen et al. [44]	18	IHC: HIF-1α	p = 0.031, r = 0.697
CTTH (DCE)				
CE	Jensen et al. [44]**	18	IHC: VEGF	p = 0.034, r = 0.599
Edema	Jensen et al. [44]	18	IHC: VEGF	p < 0.0001, r = 0.973
TTP (DSC)				
Tumor and edema	Qin et al.[49]	28	18F-FMISO PET	p < 0.001, r = 0.068
	Huang et al. [43]	33	18F-FMISO PET	ns
Peakmap (DSC)				
Tumor and edema	Qin et al.[49]	28	18F-FMISO PET	p < 0.001, r = 0.175
Peak height (DSC)				
CE	Barajas et al. [38]	51 (35)*	IHC: factor VIII	p = 0.005

AUC, area under the curve of DCE signal; CE, contrast-enhancing portion of the tumor; HIF1-α, hypoxia inducible factor 1 subunit alpha; IHC, immunohistochemistry; NE, non-contrast-enhancing portion of the tumor; TTP, time to peak; VEGF, vascular endothelial growth factor; VOI, volume-of-interest; 18F-fluoromisonidazole positron emission tomography.
* The number in between brackets is the number of subjects in whom DSC imaging was obtained, and it is this number was used for data analyses.
** Jensen et al further divided the contrast-enhancing VOI into an active tumor VOI and a hypoxic penumbra VOI, which is defined as the contrast-enhancing region surrounding the central necrosis. Findings were reported separately. This table lists findings from the active tumor VOI under the CE VOI.
Table summarizing data on transit time related measurements. Authors reported on data obtained from the contrast-enhancing portion of the tumor (CE), the non-contrast-enhancing portion of the tumor (NE), the entire tumor (CE + NE), or the tumor with surrounding edema. Gold standard methods used for comparison are shown. Transit time related measurements mostly seem to be related to gold standard hypoxia methods, except for washout rates where non-significant findings are underlined.

Discussion

Magnetic Resonance Imaging measures for tissue hypoxia have generally been identified by studies investigating subjects with cerebrovascular disease, in which tissue hypoxia is caused by a decreased cerebral perfusion pressure, resulting in autoregulation-driven vasodilation to maintain oxygen metabolism and nutrient supply to the tissue. When the oxygen demand exceeds supply at the vessel's maximum dilatory capacity, more oxygen will be extracted, reflected by an increase in OEF [61]. Compared to studies of non-neoplastic cerebrovascular disease, in situ studies evaluating MRI markers of hypoxia in human brain tumors are scarce. Tumor cells have a heightened metabolic activity, making brain tumors more prone to hypoxia than surrounding tissue [62]. Hypoxia-induced neoangiogenesis generally leads to elevated tumor blood flow. However, human glioblastoma studies have demonstrated multidirectional changes to tumor blood flow; some documented increased blood flow, whereas others found decreased blood flow with more prominent necrosis and neoangiogenesis [63,64]. Therefore, it is unclear whether the established MRI measures of tissue hypoxia in cerebrovascular disease can be interpreted similarly in a tumoral hypoxic environment.

In our review of published data, we found validation studies encompassing a wide range of MRI sequences, including conventional, diffusion-weighted, perfusion-weighted, and quantitative MRI (qMRI) techniques. From our extraction, qMRI-derived measures seem to be most promising in assessing tumor hypoxia. MRI surrogates for tissue oxygenation, including R2′ [58], T2′ [46], T2* [46], OEF [48,56,59] and CEST-MTR [58], are thought to link directly to hypoxia, and have been widely researched. Most papers found elevated OEF as a reflection of insufficient oxygen delivery in areas exhibiting tissue hypoxia or hypoxia-related neoangiogenesis. However, we did identify one paper that found a negative association between OEF and hypoxia [48], and one paper that did not find the two to be associated [59]. This may be explained by chaotic and ineffective tumor vasculature with neoangiogenesis [3]. Vaupel et al. described significant arterio-venous shunt within tumor vasculature, wherein the absence of a capillary bed can limit oxygen diffusion [65]. Similarly, Ostergaard et al. demonstrated that tumor neoangiogenesis can cause an increase in CTTH allowing for less oxygen diffusion and, therefore, decreased OEF [66]. Overall, qMRI seems promising, but applicability is limited to research institutes as the MRI sequences and processing tools are generally not available in diagnostic imaging centers.

Routinely performed in routine patient care, conventional imaging and DWI-based sequences may be more easily incorporated into clinical practice. A few papers calculated signal differences between non-contrast and contrast-enhanced T1-weighted imaging as a surrogate for vascular permeability [38,46,52]. Most reported a positive association with and hypoxia and/or hypoxia-related neoangiogenesis [38,52]. This is not unexpected given that contrast enhancement may reflect tumor aggressiveness, which coincides with both tumor neoangiogenesis and hypoxia [4]. It remains to be elucidated whether this measure can distinguish neoangiogenesis with concomitant hypoxia versus normoxic neoangiogenesis.

Similarly, DWI is readily available on diagnostic scanners, and radiologists are proficient in interpreting ADC maps. Most papers investigating these measures reported a positive association between cellular density and tissue hypoxia or hypoxia-related neoangiogenesis [32,38,42,49,52]. This finding reflects the general conception that accelerated cell proliferation outgrows the vascular supply in tumors, leading to a hypoxic tumor micro-environment [67]. However, one paper reported discrepant results with a positive correlation between ADC and tumor hypoxia when both tumor and peritumoral edema were analyzed simultaneously [49]. This finding may suggests that ADC is an unreliable marker in areas with vasogenic edema [68]. Outside of the peritumoral area, ADC does seem to be a reasonable predictor of hypoxia in the tumor tissue itself.

Perfusion-weighted imaging and associated processing software are becoming more readily available on diagnostic scanners, thereby allowing for easier incorporation of the derived measures into clinical practice. Papers that reported on MRI measures of BV [38,43,44,47–49,57,60], vascular bed transit time [43,44,49,57], and permeability [43,44,48,49] related measurements mostly found a positive association with tumor hypoxia or hypoxia-related neoangiogenesis. The former finding reflects cerebrovascular disease where autoregulatory vasodilation occurs in response to tissue hypoxia [65].

The increase in transit time, on the other hand, may reflect the chaotic tumor vasculature cycling blood across the different tumor regions [65], and elevated permeability may reflect the impacted capillary wall integrity in tumor vasculature [65]. Whereas most papers reported a positive relationship between hypoxia and permeability related measurements, Jensen et al. did not find an association [44]. Compared to the other papers reporting on permeability related measurements, this study has fewer subjects, and instead of separating VOIs into CE and NE, they sub-divided CE into active tumor VOI and hypoxic penumbra VOI. Statistical power is likely limited by the smaller sample size and fewer VOI datapoints. Contrary to MRI measures of neoangiogenesis, the relationship between MRI-measured BF and hypoxia or hypoxia-related neoangiogenesis was more variable. Here, half of the papers [48,49] reported a positive association whereas the other half did not find an association [43,44]. Though elevated blood flow is expected as a compensation for tissue hypoxia [69], the conflicting findings across papers align with Watabe et al.'s report on the wide range of tumor blood flow in an animal model of glioma, which they attributed to inter-tumor heterogeneity [70].

Multiparametric MRI integrates information from different imaging sequences, genomics, and physiological markers. In this review article, we identified a few studies that assessed multiparametric MRI and found this to be predictive of tumor hypoxia and/or hypoxia-related neoangiogenesis [38–40,51,55]. Although more computationally intensive, multiparametric MRI captures multiple physiologic processes, making it more likely to outperform a single-sequence approach. Specifically, two studies employed radiomics, which assesses tumor hypoxia from conventional MRI sequences using machine-learning models [39,40]. As of now, data on radiomics is too limited to demonstrate its superiority from a single-sequence approach. A drawback of current radiomics models is the reliance on in-house data for algorithm development. To advance this field, researchers should diversify their data source by incorporating multi-institutional MRI data to allow the models to perform on imaging data from different MRI vendors and with different sequence parameters.

Despite promising results in the studies presented above, some limitations exist. First, most studies to date are performed on high grade glioma patients. It is yet unclear whether the findings translate to other tumors, such as brain metastases or lower grade gliomas. Specifically, brain metastases often display a different histopathological pattern of neuropil infiltration [71], and are more likely to enhance tumor blood supply through vessel co-option than aberrant angiogenesis [72]. Second, even though regional MRI measures were found to be associated with corresponding PET or IHC measures, there lacks true spatial 'voxel-by-voxel' analyses. For instance, MRI measures of cellular proliferation are expected to correlate with tumor hypoxia due to increased oxygen demand and insufficient vascular supply. However, one would not expect the entire area of elevated cellular proliferation to be hypoxic; rather, spatial variation is expected based upon the distance from vasculature [73]. Finally, in current data, limited sensitivity and specificity analyses have been performed which limits the ability to compare assessments amongst each other. Comparative analyses of the different MRI measures within the same patient cohort would also be beneficial and are generally sparse due to imaging time limitations.

In conclusion, data published on MRI measures as surrogates for tumor hypoxia or hypoxia-related neoangiogenesis are promising, with data mostly supporting measurements related to tissue hypoxia (T2*, T2′, R2′) and tissue perfusion (BV, vascular bed transit time, and permeability). Other techniques, such as OEF, BF, and the difference between pre- and post-contrast T1-weighted imaging, may warrant further investigations to reconcile conflicting data. ADC seems to be able to assess tumor hypoxia within the tumor itself but may not be capable of this within the peritumoral edema region. New studies should account for histopathological differences between CNS primary tumors and brain metastases. Future work should focus on comparative and sensitivity analyses between methods to identify the most accurate method for identifying tumor hypoxia using MRI. Ultimately, this technique may be adopted for outcome prognostication and treatment adjustment based upon the absence or presence of tumor hypoxia.

Declaration of competing interest

The authors declare that they have no known competing financial interests or personal relationships that could have appeared to influence the work reported in this paper.

Acknowledgements

The authors appreciate the work of Kayce Gill, Health Sciences Collections Librarian at Vanderbilt University, who helped develop the search strategy.

Appendix A. Supplementary data

Supplementary data to this article can be found online at https://doi.org/10.1016/j.ctro.2025.100940.

References

[1] Wood KA, Wong WL, Saunders MI. [64Cu]diacetyl-bis(N4-methyl-thiosemicarbazone) — a radiotracer for tumor hypoxia. *Nucl Med Biol* 2008;35(4):393–400. https://doi.org/10.1016/j.nucmedbio.2008.02.002.
[2] Hockel M, Vaupel P. Tumor hypoxia: definitions and current clinical, biologic, and molecular aspects. *JNCI J Natl Cancer Inst* 2001;93(4):266–76. https://doi.org/10.1093/jnci/93.4.266.
[3] Matuszewska K, Pereira M, Petrik D, Lawler J, Petrik J. Normalizing tumor vasculature to reduce hypoxia, enhance perfusion, and optimize therapy uptake. *Cancers* 2021;13(17):4444. https://doi.org/10.3390/cancers13174444.
[4] Abou Khouzam R, Brodaczewska K, Filipiak A, et al. Tumor hypoxia regulates immune escape/invasion: influence on angiogenesis and potential impact of hypoxic biomarkers on cancer therapies. *Front Immunol* 2021;11:613114. https://doi.org/10.3389/fimmu.2020.613114.
[5] Gilkes DM, Semenza GL, Wirtz D. Hypoxia and the extracellular matrix: drivers of tumour metastasis. *Nat Rev Cancer* 2014;14(6):430–9. https://doi.org/10.1038/nrc3726.
[6] Eckerich C, Zapf S, Fillbrandt R, Loges S, Westphal M, Lamszus K. Hypoxia can induce c-Met expression in glioma cells and enhance SF/HGF-induced cell migration. *Int J Cancer* 2007;121(2):276–83. https://doi.org/10.1002/ijc.22679.
[7] Lin X, Xiao Z, Chen T, Liang SH, Guo H. Glucose metabolism on tumor plasticity, diagnosis, and treatment. *Front Oncol* 2020;10:317. https://doi.org/10.3389/fonc.2020.00317.
[8] Tang M, Bolderson E, O'Byrne KJ, Richard DJ. Tumor hypoxia drives genomic instability. *Front Cell Dev Biol* 2021;9:626229. https://doi.org/10.3389/fcell.2021.626229.
[9] Muz B, De La Puente P, Azab F, Azab AK. The role of hypoxia in cancer progression, angiogenesis, metastasis, and resistance to therapy. *Hypoxia*. 2015:83. doi:10.2147/HP.S93413.
[10] Walsh JC, Lebedev A, Aten E, Madsen K, Marciano L, Kolb HC. The clinical importance of assessing tumor hypoxia: relationship of tumor hypoxia to prognosis and therapeutic opportunities. *Antioxid Redox Signal* 2014;21(10):1516–54. https://doi.org/10.1089/ars.2013.5378.
[11] Koritzinsky M, Wouters BG. The roles of reactive oxygen species and autophagy in mediating the tolerance of tumor cells to cycling hypoxia. *Semin Radiat Oncol* 2013;23(4):252–61. https://doi.org/10.1016/j.semradonc.2013.05.006.
[12] Gray LH, Conger AD, Ebert M, Hornsey S, Scott OCA. The concentration of oxygen dissolved in tissues at the time of irradiation as a factor in radiotherapy. *Br J Radiol* 1953;26(312):638–48. https://doi.org/10.1259/0007-1285-26-312-638.
[13] Graham K, Unger E. Overcoming tumor hypoxia as a barrier to radiotherapy, chemotherapy and immunotherapy in cancer treatment. *Int J Nanomedicine* 2018;13:6049–58. https://doi.org/10.2147/IJN.S140462.
[14] Sharma A, Arambula JF, Koo S, et al. Hypoxia-targeted drug delivery. *Chem Soc Rev* 2019;48(3):771–813. https://doi.org/10.1039/C8CS00304A.
[15] Minassian LM, Cotechini T, Huitema E, Graham CH. Hypoxia-induced resistance to chemotherapy in cancer. In: Gilkes DM, ed. *Hypoxia and Cancer Metastasis*. Vol 1136. Advances in Experimental Medicine and Biology. Springer International Publishing; 2019:123-139. doi:10.1007/978-3-030-12734-3_9.
[16] Lee N, Schoder H, Beattie B, et al. Strategy of using intratreatment hypoxia imaging to selectively and safely guide radiation dose de-escalation concurrent with chemotherapy for locoregionally advanced human papillomavirus–related oropharyngeal carcinoma. *Int J Radiat Oncol* 2016;96(1):9–17. https://doi.org/10.1016/j.ijrobp.2016.04.027.
[17] Colliez F, Gallez B, Jordan BF. Assessing tumor oxygenation for predicting outcome in radiation oncology: a review of studies correlating tumor hypoxic status and outcome in the preclinical and clinical settings. *Front Oncol* 2017:7. https://doi.org/10.3389/fonc.2017.00010.

[18] Stone HB, Brown JM, Phillips TL, Sutherland RM. Oxygen in human tumors: correlations between methods of measurement and response to therapy: summary of a workshop Held November 19-20, 1992, at the National Cancer Institute, Bethesda, Maryland. *Radiat Res* 1993;136(3):422. https://doi.org/10.2307/3578556.

[19] Lee JW, Bae SH, Jeong JW, Kim SH, Kim KW. Hypoxia-inducible factor (HIF-1)α: its protein stability and biological functions. *Exp Mol Med* 2004;36(1):1–12. https://doi.org/10.1038/emm.2004.1.

[20] Pastorekova S, Gillies RJ. The role of carbonic anhydrase IX in cancer development: links to hypoxia, acidosis, and beyond. *Cancer Metastasis Rev* 2019;38(1–2):65–77. https://doi.org/10.1007/s10555-019-09799-0.

[21] Zhang JZ, Behrooz A, Ismail-Beigi F. Regulation of glucose transport by hypoxia. *Am J Kidney Dis* 1999;34(1):189–202. https://doi.org/10.1016/S0272-6386(99)70131-9.

[22] Duffy JP, Eibl G, Reber HA, Hines OJ. No title found. *Mol Cancer* 2003;2(1):12. https://doi.org/10.1186/1476-4598-2-12.

[23] Shibuya M. Differential roles of vascular endothelial growth factor receptor-1 and receptor-2 in angiogenesis. BMBRep2 2006;39(5):469–78. https://doi.org/10.5483/BMBRep.2006.39.5.469.

[24] Basilio-de-Oliveira RP, Pannain VLN. Prognostic angiogenic markers (endoglin, VEGF, CD31) and tumor cell proliferation (Ki67) for gastrointestinal stromal tumors. *World J Gastroenterol* 2015;21(22):6924–30. https://doi.org/10.3748/wjg.v21.i22.6924.

[25] Xu Z, Li XF, Zou H, Sun X, Shen B. 18F-Fluoromisonidazole in tumor hypoxia imaging. *Oncotarget* 2017;8(55):94969–79. https://doi.org/10.18632/oncotarget.21662.

[26] Lopci E, Grassi I, Chiti A, et al. PET radiopharmaceuticals for imaging of tumor hypoxia: a review of the evidence. *Am J Nucl Med Mol Imaging* 2014;4(4):365–84.

[27] Liu T, Karlsen M, Karlberg AM, Redalen KR. Hypoxia imaging and theranostic potential of [64Cu][Cu(ATSM)] and ionic Cu(II) salts: a review of current evidence and discussion of the retention mechanisms. *EJNMMI Res* 2020;10(1):33. https://doi.org/10.1186/s13550-020-00621-5.

[28] Carlin S, Zhang H, Reese M, Ramos NN, Chen Q, Ricketts SA. A comparison of the imaging characteristics and microregional distribution of 4 hypoxia PET tracers. *J Nucl Med* 2014;55(3):515–21. https://doi.org/10.2967/jnumed.113.126615.

[29] Hu M, Zhu Y, Mu D, et al. Correlation of hypoxia as measured by fluorine-18 fluoroerythronitroimidazole (18F-FETNIM) PET/CT and overall survival in glioma patients. *Eur J Nucl Med Mol Imaging* 2020;47(6):1427–34. https://doi.org/10.1007/s00259-019-04621-z.

[30] Ogawa S, Lee T, Nayak AS, Glynn P. Oxygenation-sensitive contrast in magnetic resonance image of rodent brain at high magnetic fields. *Magn Reson Med* 1990;14(1):68–78. https://doi.org/10.1002/mrm.1910140108.

[31] An H, Lin W. Cerebral oxygen extraction fraction and cerebral venous blood volume measurements using MRI: effects of magnetic field variation. *Magn Reson Med* 2002;47(5):958–66. https://doi.org/10.1002/mrm.10148.

[32] Barajas RF, Hess CP, Phillips JJ, et al. Super-resolution track density imaging of glioblastoma: histopathologic correlation. *Am J Neuroradiol* 2013;34(7):1319–25. https://doi.org/10.3174/ajnr.A3400.

[33] Mayer P, Kraft A, Witzel HR, et al. Restricted water diffusion in diffusion-weighted magnetic resonance imaging in pancreatic cancer is associated with tumor hypoxia. *Cancers* 2020;13(1):89. https://doi.org/10.3390/cancers13010089.

[34] Rosen BR, Belliveau JW, Vevea JM, Brady TJ. Perfusion imaging with NMR contrast agents. *Magn Reson Med* 1990;14(2):249–65. https://doi.org/10.1002/mrm.1910140211.

[35] Alsop DC, Detre JA. Multisection cerebral blood flow MR imaging with continuous arterial spin labeling. *Radiology* 1998;208(2):410–6. https://doi.org/10.1148/radiology.208.2.9680569.

[36] Behar KL, Ogino T. Characterization of macromolecule resonances in the ^{1}H NMR spectrum of rat brain. *Magn Reson Med* 1993;30(1):38–44. https://doi.org/10.1002/mrm.1910300107.

[37] Ward KM, Aletras AH, Balaban RS. A new class of contrast agents for MRI based on proton chemical exchange dependent saturation transfer (CEST). *J Magn Reson* 2000;143(1):79–87. https://doi.org/10.1006/jmre.1999.1956.

[38] Barajas RF, Phillips JJ, Parvataneni R, et al. Regional variation in histopathologic features of tumor specimens from treatment-naive glioblastoma correlates with anatomic and physiologic MR Imaging. *Neuro-Oncol* 2012;14(7):942–54. https://doi.org/10.1093/neuonc/nos128.

[39] Beig N, Patel J, Prasanna P, et al. Radiogenomic analysis of hypoxia pathway is predictive of overall survival in Glioblastoma. *Sci Rep* 2018;8(1):7. https://doi.org/10.1038/s41598-017-18310-0.

[40] Beig N, Bera K, Prasanna P, et al. Radiogenomic-based survival risk stratification of tumor habitat on Gd-T1w MRI is associated with biological processes in glioblastoma. *Clin Cancer Res* 2020;26(8):1866–76. https://doi.org/10.1158/1078-0432.CCR-19-2556.

[41] Gerstner ER, Zhang Z, Fink JR, et al. ACRIN 6684: assessment of tumor hypoxia in newly diagnosed glioblastoma using 18F-FMISO PET and MRI. *Clin Cancer Res* 2016;22(20):5079–86. https://doi.org/10.1158/1078-0432.CCR-15-2529.

[42] Hino-Shishikura A, Tateishi U, Shibata H, et al. Tumor hypoxia and microscopic diffusion capacity in brain tumors: a comparison of 62Cu-Diacetyl-Bis (N4-Methylthiosemicarbazone) PET/CT and diffusion-weighted MR imaging. *Eur J Nucl Med Mol Imaging* 2014;41(7):1419–27. https://doi.org/10.1007/s00259-014-2714-x.

[43] Huang S, Michalek JE, Reardon DA, et al. Assessment of tumor hypoxia and perfusion in recurrent glioblastoma following bevacizumab failure using MRI and 18F-FMISO PET. *Sci Rep* 2021;11(1):7632. https://doi.org/10.1038/s41598-021-84331-5.

[44] Jensen RL, Mumert ML, Gillespie DL, Kinney AY, Schabel MC, Salzman KL. Preoperative dynamic contrast-enhanced MRI correlates with molecular markers of hypoxia and vascularity in specific areas of intratumoral microenvironment and is predictive of patient outcome. *Neuro-Oncol* 2014;16(2):280–91. https://doi.org/10.1093/neuonc/not148.

[45] Maralani PJ, Das S, Mainprize T, et al. Hypoxia detection in infiltrative astrocytoma: ferumoxytol-based quantitative BOLD MRI with intraoperative and histologic validation. *Radiology* 2018;288(3):821–9. https://doi.org/10.1148/radiol.2018172601.

[46] Maurer GD, Tichy J, Harter PN, et al. Matching quantitative MRI parameters with histological features of treatment-naïve IDH wild-type glioma. *Cancers* 2021;13(16):4060. https://doi.org/10.3390/cancers13164060.

[47] Da Ponte KF, Berro DH, Collet S, et al. In vivo relationship between hypoxia and angiogenesis in human glioblastoma: a multimodal imaging study. *J Nucl Med* 2017;58(10):1574–9. https://doi.org/10.2967/jnumed.116.188557.

[48] Preibisch C, Shi K, Kluge A, et al. Characterizing hypoxia in human glioma: a simultaneous multimodal MRI and PET study. *NMR Biomed* 2017;30(11):e3775.

[49] Qin J, Tang Y, Wang B. Regional 18F-fluoromisonidazole PET images generated from multiple advanced MR images using neural networks in glioblastoma. *Medicine (Baltimore)* 2022;101(30):e29572. https://doi.org/10.1097/MD.0000000000029572.

[50] Ratai EM, Zhang Z, Fink J, et al. ACRIN 6684: Multicenter, phase II assessment of tumor hypoxia in newly diagnosed glioblastoma using magnetic resonance spectroscopy. Monleon D, ed. *PLOS ONE*. 2018;13(6):e0198548. doi:10.1371/journal.pone.0198548.

[51] Shimizu Y, Kudo K, Kameda H, et al. Prediction of hypoxia in brain tumors using a multivariate model built from MR imaging and ^{18}F-fluorodeoxyglucose accumulation data. *Magn Reson Med Sci* 2020;19(3):227–34. https://doi.org/10.2463/mrms.mp.2019-0049.

[52] Shu C, Wang J. The relationship between MRI quantitative parameters and the expression of hypoxia inducible factor-1 alpha in cerebral astrocytoma. *Clin Neurol Neurosurg* 2017;153:14–9. https://doi.org/10.1016/j.clineuro.2016.11.013.

[53] Spanberger T, Berghoff AS, Dinhof C, et al. Extent of peritumoral brain edema correlates with prognosis, tumoral growth pattern, HIF1a expression and angiogenic activity in patients with single brain metastases. *Clin Exp Metastasis* 2013;30(4):357–68. https://doi.org/10.1007/s10585-012-9542-9.

[54] Swanson KR, Chakraborty G, Wang CH, et al. Complementary but distinct roles for MRI and ^{18} F-fluoromisonidazole PET in the assessment of human glioblastomas. *J Nucl Med* 2009;50(1):36–44. https://doi.org/10.2967/jnumed.108.055467.

[55] Szeto MD, Chakraborty G, Hadley J, et al. Quantitative metrics of net proliferation and invasion link biological aggressiveness assessed by MRI with hypoxia assessed by FMISO-PET in newly diagnosed glioblastomas. *Cancer Res* 2009;69(10):4502–9. https://doi.org/10.1158/0008-5472.CAN-08-3884.

[56] Tóth V, Förschler A, Hirsch NM, et al. MR-based hypoxia measures in human glioma. *J Neurooncol* 2013;115(2):197–207. https://doi.org/10.1007/s11060-013-1210-7.

[57] Xie Q, Wu J, Du Z, et al. DCE-MRI in human gliomas. *Acad Radiol* 2019;26(2):179–87. https://doi.org/10.1016/j.acra.2018.04.015.

[58] Yao J, Chakhoyan A, Nathanson DA, et al. Metabolic characterization of human IDH mutant and wild type gliomas using simultaneous pH- and oxygen-sensitive molecular MRI. *Neuro-Oncol*. 2019:noz078. doi:10.1093/neuonc/noz078.

[59] Arzanforoosh F, Van der Velden M, Berman AJL, et al. MRI-based assessment of brain tumor hypoxia: correlation with histology. *Cancers* 2023;16(138). https://doi.org/10.3390/cancers16010138.

[60] Sadeghi N, Salmon I, Decaestecker C, et al. Stereotactic comparison among cerebral blood volume, methionine uptake, and histopathology in brain glioma. *AJNR Am J Neuroradiol* 2007;28(3):455–61.

[61] Derdeyn CP, Videen TO, Yundt KD, et al. Variability of cerebral blood volume and oxygen extraction: stages of cerebral haemodynamic impairment revisited. *Brain* 2002;125(3):595–607. https://doi.org/10.1093/brain/awf047.

[62] Park JH, Lee HK. The role of hypoxia in brain tumor immune responses. *Brain Tumor Res Treat* 2023;11(1):39. https://doi.org/10.14791/btrt.2022.0043.

[63] Crocker M, Saadoun S, Jury A, et al. Glioblastoma blood flow measured with stable xenon CT indicates tumor necrosis, vascularity, and brain invasion. *Neuro-Oncol* 2012;14(5):641–8. https://doi.org/10.1093/neuonc/nos063.

[64] Peter Vaupel F, Kallinowski PO. Blood flow, oxygen and nutrient supply, and metabolic microenvironment of human tumors: a review. *Cancer Res* 1989;49(23):6449–65.

[65] Vaupel P. Tumor microenvironmental physiology and its implications for radiation oncology. *Semin Radiat Oncol* 2004;14(3):198–206. https://doi.org/10.1016/j.semradonc.2004.04.008.

[66] Østergaard L, Tietze A, Nielsen T, et al. The relationship between tumor blood flow, angiogenesis, tumor hypoxia, and aerobic glycolysis. *Cancer Res* 2013;73(18):5618–24. https://doi.org/10.1158/0008-5472.CAN-13-0964.

[67] Li Y, Zhao L, Li XF. Hypoxia and the tumor microenvironment. *Technol Cancer Res Treat* 2021;20. https://doi.org/10.1177/15330338211036304.153303382110363.

[68] Andersen C, Jensen FT. Differences in blood-tumour-barrier leakage of human intracranial tumours: quantitative monitoring of vasogenic oedema and its response to glucocorticoid treatment. *Acta Neurochir (wien)* 1998;140(9):919–24. https://doi.org/10.1007/s007010050194.

[69] Powers WJ. Cerebral hemodynamics in ischemic cerebrovascular disease. *Ann Neurol* 1991;29(3):231–40. https://doi.org/10.1002/ana.410290302.

[70] Watabe T, Kanai Y, Ikeda H, et al. Quantitative evaluation of oxygen metabolism in the intratumoral hypoxia: 18F-fluoromisonidazole and 15O-labelled gases

inhalation PET. *EJNMMI Res* 2017;7(1):16. https://doi.org/10.1186/s13550-017-0263-6.

[71] Berghoff AS, Rajky O, Winkler F, et al. Invasion patterns in brain metastases of solid cancers. *Neuro-Oncol* 2013;15(12):1664–72. https://doi.org/10.1093/neuonc/not112.

[72] Donnem T, Hu J, Ferguson M, et al. Vessel co-option in primary human tumors and metastases: an obstacle to effective anti-angiogenic treatment? *Cancer Med* 2013;2(4):427–36. https://doi.org/10.1002/cam4.105.

[73] Sun H, Li Y, Zhang Y, et al. The relevance between hypoxia-dependent spatial transcriptomics and the prognosis and efficacy of immunotherapy in claudin-low breast cancer. *Front Immunol* 2023;13:1042835. https://doi.org/10.3389/fimmu.2022.1042835.

[74] Lu H, Ge Y. Quantitative evaluation of oxygenation in venous vessels using T2-Relaxation-Under-Spin-Tagging MRI. *Magn Reson Med* 2008;60(2):357–63. https://doi.org/10.1002/mrm.21627.

[75] An H, Lin W. Impact of intravascular signal on quantitative measures of cerebral oxygen extraction and blood volume under normo- and hypercapnic conditions using an asymmetric spin echo approach. *Magn Reson Med* 2003;50(4):708–16. https://doi.org/10.1002/mrm.10576.

[76] Waddle SL, Garza M, Ying C, et al. Vascular space occupancy asymmetric spin echo (VASO-ASE) for non-invasive quantification of cerebral oxygen extraction fraction. *Magn Reson Med* 2023;90(1):211–21. https://doi.org/10.1002/mrm.29618.